Green Chemistry

ARTICLE

Engineering the acidity and accessibility of the zeolite ZSM-5 for efficient bio-oil upgrading in catalytic pyrolysis of lignocellulose

Received 00th January 20xx,
Accepted 00th January 20xx

DOI: 10.1039/x0xx00000x

www.rsc.org/

Héctor Hernando,[a] Ana M. Hernández-Giménez,[b] Cristina Ochoa-Hernández,[c,†] Pieter C. A. Bruijnincx,[b] Klaartje Houben,[d] Marc Baldus,[d] Patricia Pizarro,[a,e] Juan M. Coronado,[a] Javier Fermoso,[a] Jiří Čejka,[c] Bert M. Weckhuysen,[b] David P. Serrano[a,e]*

The properties of the zeolite ZSM-5 have been optimised for the production and deoxygenation of the bio-oil* (bio-oil on water-free basis) fraction by lignocellulose catalytic pyrolysis. Two ZSM-5 supports possessing high mesopore/external surface area, and therefore enhanced accessibility, have been employed to promote the conversion of the bulky compounds formed in the primary cracking of lignocellulose. These supports are a nanocrystalline material (n-ZSM-5) and a hierarchical sample (h-ZSM-5) of different Si/Al ratios and acid site concentrations. Acidic features of both zeolites have been modified and adjusted by incorporation of ZrO_2, which has a significant effect on the concentration and distribution of both Brønsted and Lewis acid sites. These materials have been tested in the catalytic pyrolysis of acid-washed wheat straw (WS-ac) using a two-step (thermal/catalytic) reaction system at different catalyst/biomass ratios. The results obtained have been assessed in terms of oxygen content, energy yield and composition of the produced bio-oil*, taking also into account the selectivity towards the different deoxygenation pathways. The ZrO_2/n-ZSM-5 sample showed remarkable performance in the biomass catalytic pyrolysis, as a result of the appropriate combination of accessibility and acidic properties. In particular, modification of the zeolitic support acidity by incorporation of highly dispersed ZrO_2 effectively decreased the extent of secondary reactions, such as severe cracking and coke formation, as well as promoted the conversion of the oligomers formed initially by lignocellulose pyrolysis, thus sharply decreasing the proportion of the components not detected by GC-MS in the upgraded bio-oil*.

Introduction

Biomass catalytic fast pyrolysis (CFP) is considered one of the most feasible routes for the production of liquid biofuels from lignocellulose, as it is a relatively simple process that takes place at atmospheric pressure, moderate temperatures and with short residence times [1,2]. In addition to the liquid fraction (bio-oil), gases and a carbonaceous solid (char) are also produced. Bio-oil is viewed as an interesting product that could be applied for both biofuels and bio-based chemicals production [3,4]. However, it contains a large variety of oxygenated compounds and significant amounts of water, which provides it with a number of undesired properties, such as low calorific value, immiscibility with fossil-derived fuels and acid pH (corrosiveness) [1]. Moreover, bio-oil is not a stable product since even at room temperature it undergoes a number of reactions and transformations upon storage, which usually provokes phase separation and formation of solids [3,5]. Accordingly, the bio-oil produced by thermal degradation of lignocellulose should be regarded as a low-quality fuel with limited economic value [6].

In recent years, two main chemical routes have been proposed for improving the bio-oil properties: catalytic pyrolysis using acid solids, and hydrodeoxygenation over metal-containing catalysts [7,8]. Catalytic pyrolysis presents the advantages of operation at the atmospheric pressure and not consuming external hydrogen, although it is limited by extensive formation of carbonaceous deposits leading to catalyst deactivation and reduction in the bio-oil yield [9–13]. On the other hand, other catalytic transformations have been recently explored for bio-oil upgrading based on the use of catalysts with ketonization and aldol condensation activities, which allow the oxygen content of the bio-oil to be reduced with simultaneous C-C bond formation, hence increasing the molecular weight of the species present in the bio-oil [14–17].

Bio-oil upgrading by catalytic pyrolysis can be performed in-situ or ex-situ regarding the pyrolysis reactor [2,18,19]. The second configuration is more convenient since in this case the direct contact of the catalyst with the raw biomass is avoided,

[a] Thermochemical Processes Unit, IMDEA Energy Institute, 28935, Móstoles, Madrid, Spain
[b] Inorganic Chemistry and Catalysis, Debye Institute for Nanomaterials Science, Utrecht University, Universiteitsweg 99, 3584 CG Utrecht, The Netherlands
[c] J. Heyrovský Institute of Physical Chemistry, Czech Academy of Sciences, v.v.i., 182 23, Prague 8, Czech Republic
[d] NMR Spectroscopy, Bijvoet Center for Biomolecular Research, Department of Chemistry, Utrecht University, Padualaan 8, 3584 CH Utrecht, The Netherlands
[e] Chemical and Environmental Engineering Group, ESCET, Rey Juan Carlos University, 28933, Móstoles, Madrid, Spain
† Current affiliation address: Department of Heterogeneous Catalysis, Max-Planck-Institut für Kohlenforschung, 45470, Mülheim an der Ruhr, Germany

limiting at least partially the catalyst deactivation. In addition, both thermal and catalytic steps can be operated under different reaction conditions affording a more efficient biomass conversion and bio-oil upgrading [2,9]. Indeed, it has been earlier shown that the optimum temperatures for biomass pyrolysis and bio-oil catalytic conversion differ significantly, demonstrating the convenience of ex-situ reaction systems for lignocellulose catalytic pyrolysis [9].

Among solid catalysts employed in biomass catalytic pyrolysis, zeolites exhibited a remarkable performance in terms of bio-oil quality and deoxygenation degree [20,21]. In particular, ZSM-5 zeolite has led to promising results, selectively promoting the formation of aromatic hydrocarbons, hence opening the possibility of using the obtained upgraded bio-oil in the formulation of advanced biofuels [22–25]. This effect has been mainly related to the medium size of the micropores and strong acidity of ZSM-5 zeolite [26]. However, the use of this zeolite in biomass catalytic pyrolysis leads to low bio-oil yields as it also suffers from hindered accessibility to the active sites, coke deposition over the catalyst and occurrence of severe cracking reactions that promote the formation of gaseous hydrocarbons [18].

A strong research effort has been devoted to improve the ZSM-5 behaviour in biomass catalytic pyrolysis. Thereby, the ZSM-5 properties have been modified by reduction of the crystal size [11,23,27], introduction of a secondary porosity in the mesopore range [11,23,28,29] or use of 2D ZSM-5 materials in order to increase the accessibility of the compounds present in the bio-oil vapours to the active sites [30]. Likewise, the addition of metals to ZSM-5 zeolite has been extensively investigated to increase the aromatisation activity and/or to decrease the coke formation during biomass pyrolysis. Thus, numerous works have been published using ZSM-5 zeolites, modified by incorporating a variety of elements, such as Pt, Pd, Ni, Ga, Mg, Zn, Co and Fe, in the catalytic pyrolysis of different lignocellulosic feedstock [10,22,31–39].

On the other hand, ZrO_2-based catalysts have been reported in the past years as materials with suitable catalytic properties for different biomass transformations, including not just biomass catalytic pyrolysis, but also other reactions of interest for the conversion of biomass-derived intermediates, such as ketonization [14], aldol condensation [40–42] and esterification [42,43]. In contrast, almost no examples can be found in the literature exploring the modification of ZSM-5 with ZrO_2 for biomass catalytic pyrolysis. A rare example is provided by Li et al., who have recently investigated the biomass catalytic pyrolysis over Fe-, Zr- and Co-modified ZSM-5 zeolites [32,39], showing some positive effects of the incorporation of these elements in terms of product distribution, but providing no information on the deoxygenation degree of the bio-oil neither on its energy yield and on other relevant properties related to the level of upgrading achieved. Moreover, the zeolitic support used by these authors is a standard ZSM-5 of micrometer crystal size and, therefore, with very limited mesopore/external surface and accessibility, which may explain the relatively small effect seen upon zeolite modification.

In this context, the present work aims at adjusting the ZSM-5 properties to overcome its limitations in biomass catalytic pyrolysis for the production of upgraded bio-oil. Thereby, two main properties of the ZSM-5 zeolite are considered in the catalyst engineering strategy: high accessibility and tailored acidity. Thus, enhanced accessibility to the active sites was ensured by using two different non-standard ZSM-5 zeolites: a hierarchical ZSM-5 sample prepared by desilication (h-ZSM-5) and a nanocrystalline ZSM-5 material (n-ZSM-5). Both zeolites have high mesopore/external surface areas and reduced diffusional pathway lengths, properties expected to promote the conversion of the bulky molecules present in the bio-oil vapours. In addition to the variation of the Si/Al ratio, the incorporation of highly dispersed ZrO_2 over these ZSM-5 samples is here reported as a very efficient strategy for modulating and complementing the zeolite acidic features and improving their performance in biomass catalytic pyrolysis, as demonstrated by a variety of characterization techniques. The results obtained in the catalytic tests have been assessed using a quite complete set of parameters, including composition and mass yield of the different fractions obtained in the pyrolysis process (bio-oil, gases, water, char and coke formed over the catalyst), deoxygenation pathways selectivity and energy yield of the produced bio-oil.

Experimental

Detailed information about the catalysts preparation and characterization techniques, as well as on the procedure and set up employed for the biomass catalytic pyrolysis tests, is provided as Supporting Information.

Results and discussion

Catalysts properties

Basic characterization of the catalysts. The parent ZSM-5 samples used in this work possess very different Al content with values of the Si/Al molar ratios of 42 and 12 for the n-ZSM-5 and h-ZSM-5 samples, respectively (Table 1). The high Al content of the h-ZSM-5 zeolite is caused by the NaOH desilication treatment employed to generate the secondary porosity present in this material, which provokes extensive silica extraction from the zeolite framework.

High-angle X-ray diffraction patterns of the ZSM-5 samples (Fig. S1) exhibited typical diffraction lines of highly crystalline zeolites with MFI topology. The incorporation of ZrO_2 to the supports had no evident effect on their crystallinity. The fact that the impregnated samples did not exhibit diffraction peaks of pure zirconium oxide phases is indicative of the existence of either ZrO_2 particles with very small size and homogeneous dispersion over the ZSM-5 supports or the absence of crystalline ZrO_2 particles. In line with the XRD data, Raman spectroscopy also did not show any evidence for the presence of a perfectly crystalline ZrO_2 component (Fig. S2). Thus, the main broad band seen in the Raman spectra for both Zr-containing samples at 381 cm^{-1} coincides with a vibration of monoclinic ZrO_2, but other bands expected for this phase, e.g. at

Green Chemistry

ARTICLE

Table 1 Physicochemical properties of the catalysts

Sample	Si/Al[a]	ZrO_2 (wt%)	S_{BET}[b] (m^2/g)	$S_{MES+EXT}$[c] (m^2/g)	S_{MIC}[d] (m^2/g)	V_T[e] (cm^3/g)	V_{MIC}[f] (cm^3/g)	C_B (mmol/g)	C_L (mmol/g)
h-ZSM-5	12	---	447	206	241	0.584	0.144	0.192	0.179
ZrO_2/h-ZSM-5	12	7.8	362	197	165	0.550	0.100	0.091	0.083
n-ZSM-5	42	---	445	133	312	0.512	0.186	0.134	0.061
ZrO_2/n-ZSM-5	42	9.2	413	100	313	0.420	0.190	0.128	0.100

[a] Quantities in molar ratio; [b] BET surface area; [c] Mesopore + external surface area; [d] Micropore surface area; [e] Total pore volume at $P/P_0 \approx 0.98$; [f] Micropore volume. All textural and acidic properties are expressed per gram of zeolitic support in the sample.

475, 615 and 637 cm^{-1} are hardly or not detected [44,45]. Orthorhombic and tetragonal ZrO_2 phases can also be discarded, as they would show significantly different Raman features than those detected for the ZrO_2/h-ZSM-5 and ZrO_2/n-ZSM-5 samples [46,47]. These results show that the ZrO_2 present over the zeolitic support is poorly crystalline, most likely amorphous.

The textural properties of the catalysts were determined from the Ar adsorption isotherms at −186 °C applying the NL-DFT model, which allowed the contribution of the zeolite micropores and that of the mesopore/external surface to be distinguished (Table 1). Both parent samples present similar BET areas and a significant amount of mesopore/external surfaces, as expected taking into account their nanocrystalline and hierarchical features. This effect is more pronounced in the case of the h-ZSM-5 sample ($S_{MES+EXT}$ = 206 m^2/g), confirming that the desilication treatment was very effective in generating mesopores. After Zr incorporation, some attenuation of the textural properties was observed for both ZSM-5 samples. This variation was more accentuated for h-ZSM-5, whose micropore surface area and micropore volume were especially affected (32% of reduction), indicating that part of the Zr species are located within the zeolite micropores. In contrast, for the n-ZSM-5 catalyst Zr incorporation had a stronger effect on the mesopore+external surface (reduction of 25%) while no reduction is observed in the micropore one; hence, it can be concluded that in this sample the ZrO_2 is mainly located over the outer part of the zeolite nanocrystals rather than within the micropores.

TEM and SEM examination of the h-ZSM-5 zeolite (Fig. 1a and S3a, respectively) showed coffin-shaped crystallites with sizes in the micrometer range (about 1 – 2.5 μm). Moreover, the presence of a high proportion of voids within the crystals is clearly observed, confirming the effectiveness of the desilication treatment for generating mesopores (see high resolution images in Fig. 1a). After zirconia impregnation, no apparent differences can be observed in the hierarchical zeolite catalysts (Fig. 1b), except for a rougher appearance for the Zr-promoted sample (Fig. S3b). Yet, SEM-EDX dot-mapping on ZrO_2/h-ZSM-5 sample showed Zr (Fig. S3b_3) to be homogeneously dispersed over the crystallites, most likely being located within the zeolite micropores, with a Si/Zr molar ratio of ca. 12 (Fig. S4). On the other hand, TEM and SEM images of the n-ZSM-5 zeolite sample showed aggregates between 20-50 μm in size, consisting of crystallites of about 25-50 nm and thus confirming its nanocrystallinity (Fig. 1c and S3c, respectively). The Zr-promoted nanozeolite crystals appeared to be uniformly coated by ZrO_2 nanoparticles of rugged morphology located more on the external surface of the zeolite crystals (Fig. 1d). The SEM-EDX image of the ZrO_2/n-ZSM-5 (Fig. S3d) indicated that the Zr (d_3) is evenly distributed over the sample, as evidenced by EDX dot-mapping, with a Si/Zr molar ratio of ca. 14 (Fig. S4), which is very close to the overall one (Si/Zr = 15).

Al environment and acidity. Aluminium speciation in the different catalyst samples was examined by solid-state ^{27}Al ssMAS (Fig. 2a,b) and ^{27}Al MQ ssMAS NMR (Fig. 2c,d) analyses. For the h-ZSM-5 sample, in addition to framework tetrahedral (Al^{IV}, 53 ppm, A) and extra-framework octahedral (Al^{VI}, 0 ppm, E) Al [48–50], some penta-coordinated extra-framework Al (Al^{V}; C) is also present, as detected at ca. 30 ppm [51]. Other minor resonances at ca. 40 ppm (B) and -10 ppm (F) correspond to distorted tetrahedral and octahedral Al, respectively, as deduced from the 2D MQ ssMAS NMR spectra (Fig. 2c). This variety of Al environments in the h-ZSM-5 sample is a direct consequence of the desilication treatment applied for the generation of mesoporosity, lowering the Si/Al ratio and generating extraframework Al. ZrO_2 addition (green series in Fig. 2) led to slight distortions of the different signals, in particular of the one associated with species C, whereas a shoulder (species D) is observed in the region of octahedral Al environments. These changes denote the existence of interactions between the Zr and some of the Al species of the zeolite. On the other hand, Zr^{4+} incorporation into the framework is excluded, as this would have resulted in more significant distortions and the formation of defects in the structure. The 1D Al spectra of h-ZSM-5 (Fig. S5a) and ZrO_2/h-

Green Chemistry

ARTICLE

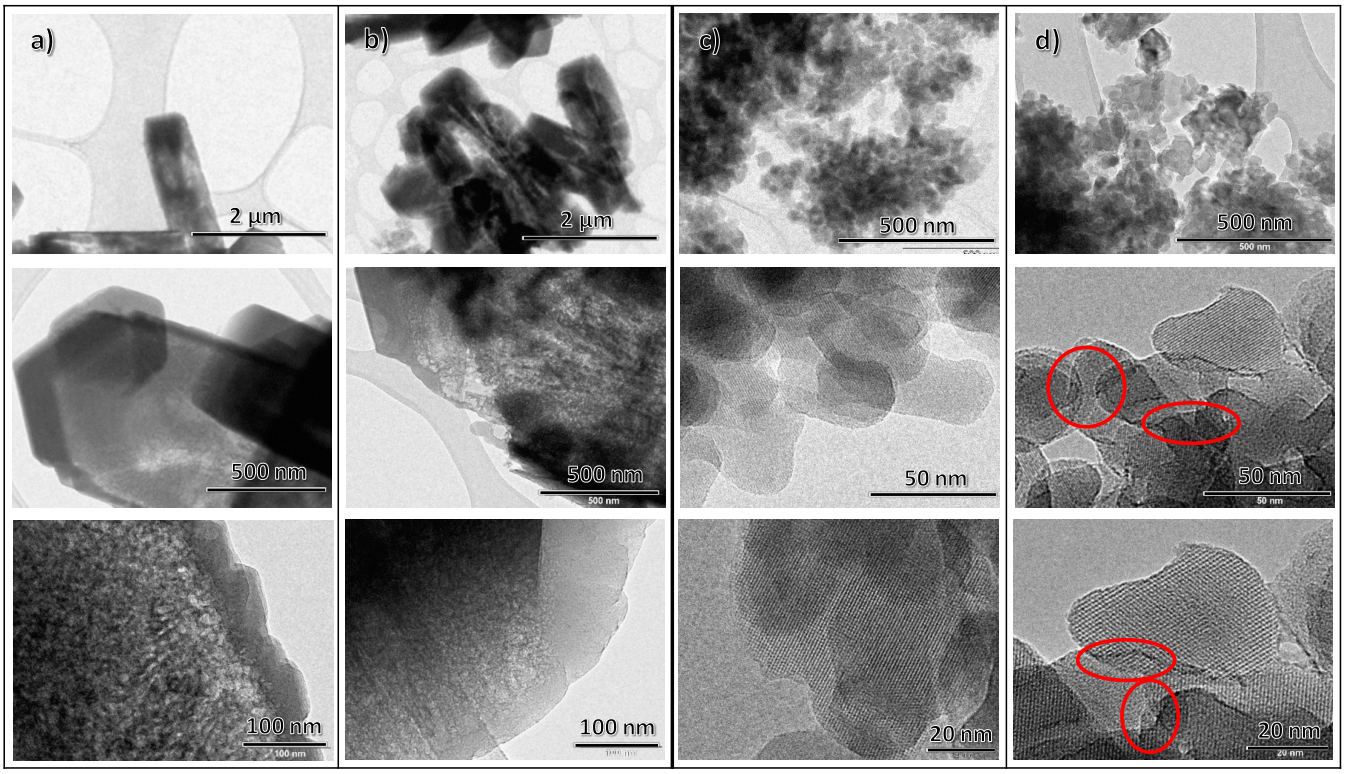

Fig. 1 TEM images of h-ZSM-5 (a), ZrO_2/h-ZSM-5 (b), n-ZSM-5 (c) and ZrO_2/n-ZSM-5 (d). The marked areas in d correspond to regions rich in ZrO_2 nanoparticles.

ZSM-5 samples (Fig. S5b) were fitted, with the number and peak maxima of the Gaussians having been obtained from the MQ MAS spectra (see Table S1). The ratio between framework and extra-framework Al species is also presented in Table S1, suggesting a small drop in framework Al sites after Zr incorporation [48,50]. In strong contrast with the h-ZSM-5 catalyst, the n-ZSM-5 sample, which was not subjected to any desilication process, almost exclusively showed tetrahedral Al species located at 54 ppm (A, blue series Fig. 2e, f) and very little octahedral Al at 0 ppm (Al^{VI}, E). The same is seen after ZrO_2 addition (red series in Fig. 2e), with the spectrum of ZrO_2/n-ZSM-5 being practically identical to the one obtained for the pure zeolite. In this case, no interactions between any Zr species and Al seem to be detected, which is consistent with the ZrO_2 location on the external surface of this sample, as suggested by TEM and by Ar physisorption.

The concentration, type and strength of the acid sites have been determined by pyridine adsorption at 150 °C followed by FTIR (Py-FTIR). Table 1 summarizes the results obtained for the different samples in terms of Brønsted and Lewis acid sites concentration (BAS and LAS, respectively). The h-ZSM-5 sample possesses a higher acid sites concentration in line with its lower Si/Al ratio. The incorporation of ZrO_2 to h-ZSM-5 support caused a significant decrease in the concentration of both BAS and LAS, which may be due to a direct interaction between the Zr species and the acid sites and/or to a partial blockage of the zeolite micropores as above denoted from the variation of the textural properties. In the case of the n-ZSM-5 support, the addition of ZrO_2 provoked just a slight decrease in the BAS concentration. However, an increase is observed in the content of LAS. Thus, the ZrO_2/n-ZSM-5 material showed higher LAS concentration than the parent support, denoting that additional LAS were generated upon ZrO_2 incorporation. In order to analyse this last effect in more detail, Fig. 3 compares the FTIR spectra of the n-ZSM-5 and ZrO_2/n-ZSM-5 samples before and after pyridine adsorption followed by evacuation at different temperatures. In the hydroxyl stretching vibration region (Fig. 3a and c), it is observed that before adsorption both samples display two bands at 3745 cm^{-1} and 3610 cm^{-1} assigned to terminal silanol groups and acidic bridging OH groups (Si-OH-Al), respectively. The intensity of these bands was slightly lower in the case of ZrO_2/n-ZSM-5. After pyridine adsorption, these bands disappeared, with new

Green Chemistry

ARTICLE

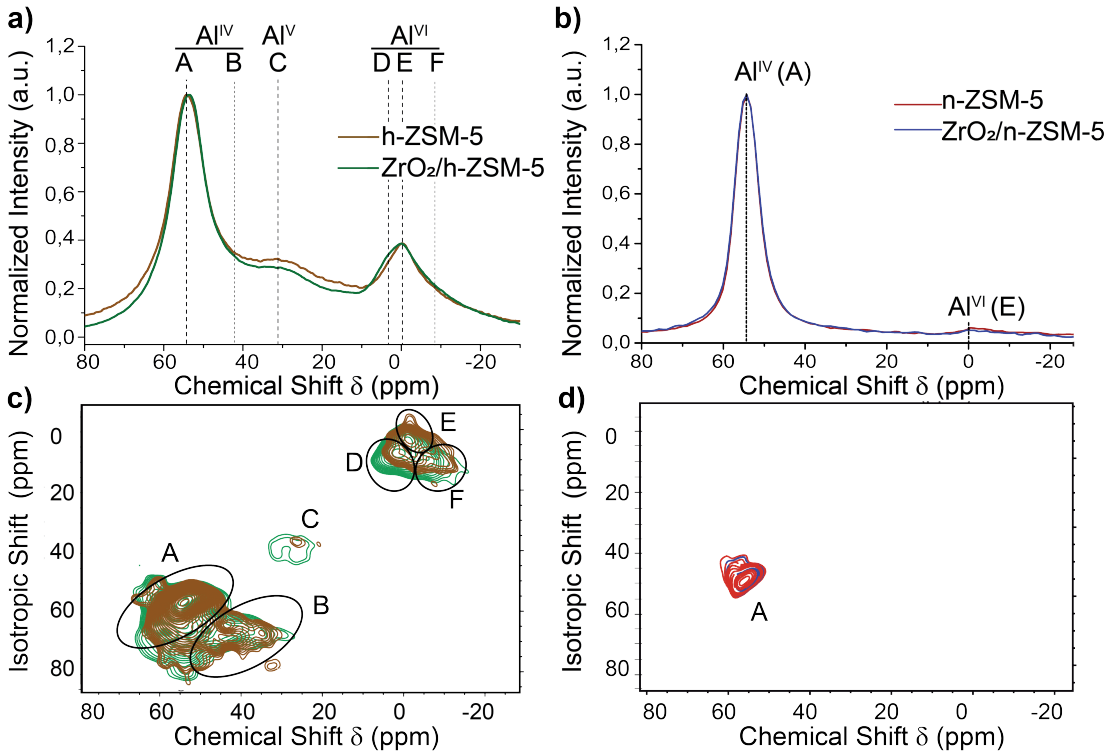

Fig. 2 Normalized ^{27}Al MAS ssNMR (a,b) and overlaid ^{27}Al MQ ssMAS NMR (c,d) spectra of h-ZSM-5 (orange) and ZrO_2/h-ZSM-5 (green) (a,c), and n-ZSM-5 (red) and ZrO_2/n-ZSM-5 (blue) (b,d). A to F correspond to the different contributing Al species which compose the NMR spectrum (see Fig. S5).

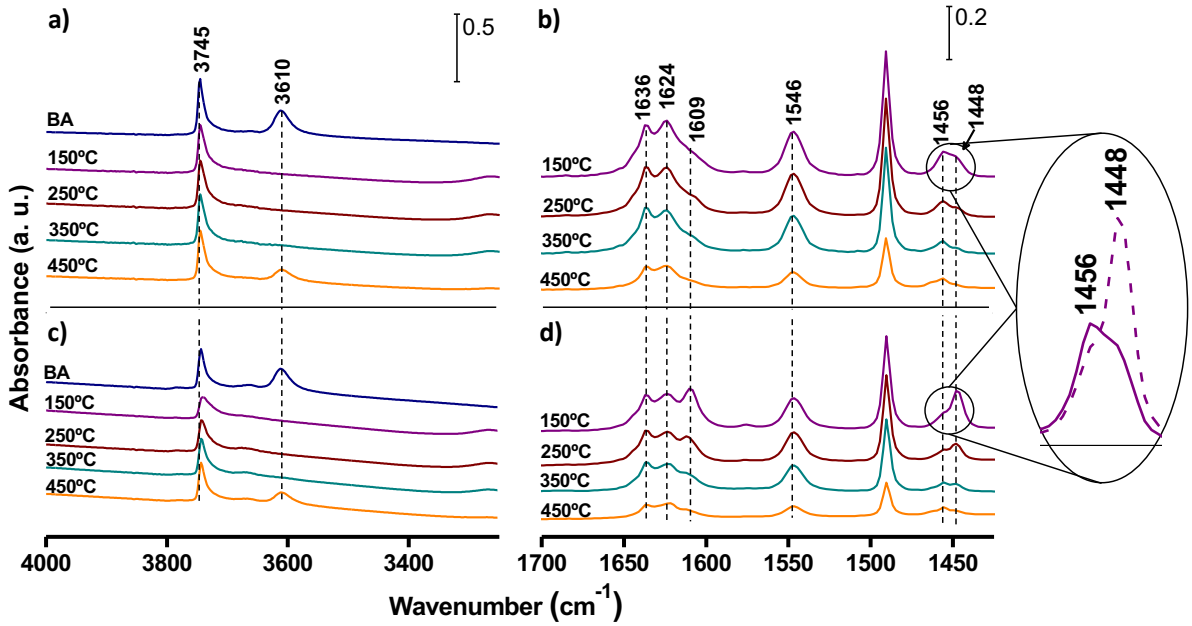

Fig. 3 FTIR spectra of the OH stretching vibration (a and c) and the pyridine vibration regions (b and d) for n-ZSM-5 (a and b) and ZrO_2/n-ZSM-5 (c and d).

Green Chemistry

ARTICLE

ones emerging ascribed to different ring vibration modes of the pyridine interacting with the acid sites (Fig. 3b and d): υ_{8a} (1650-1600 cm^{-1}) and υ_{19b} (1580-1430 cm^{-1}). The new bands at 1636 cm^{-1} and 1546 cm^{-1} correspond to pyridine chemisorbed on the BAS of n-ZSM-5 (pyridinium ions, PyH^+), whereas those at 1624 cm^{-1} and 1456 cm^{-1} are attributed to pyridine adsorbed on Al^{3+} ions in tetrahedral environment (Lewis acidity, PyL). Moreover, two additional bands at 1609 cm^{-1} and 1448 cm^{-1} could be distinguished for the ZrO_2/n-ZSM-5 sample, which can be assigned to the presence of pyridine interacting with LAS associated to Zr species [52]. The relative strength of the acid sites can be deduced from the evolution of the pyridine desorption with the temperature. Thus, both samples exhibited a similar behaviour in terms of BAS in the range of evacuation temperatures from 150 °C up to 350 °C. However, the intensity of the bands at 1609 cm^{-1} and 1448 cm^{-1}, related to ZrO_2, decreased faster upon increasing the temperature than those associated with the zeolitic LAS (Fig. 3d), indicating that the former are of lower strength.

Selective staining of the materials with 4-fluorostyrene (Scheme S1a) was used to probe the (local) Brønsted acidity properties of the zeolites, before and after ZrO_2 addition. On Brønsted sites of sufficient acidity, 4-fluorostyrene reacts to give (cyclic) dimers (see Scheme S1b, compounds 3-5), or higher oligomers, such as trimer (6) species. The formation of cyclic species (7) over the linear oligomers (5, 6) is favoured over stronger Brønsted acid sites (BAS). The in-situ UV-Vis absorption bands recorded for the different samples are displayed in Fig. 4, with the time evolution of selected wavelengths in the in-situ CFM emission spectra shown in Fig. S6 [53,54]. Here, it should be noted that the absorption and emission bands evolve in the same manner.

The band profiles and peak positions of the maxima seen are similar for all catalyst samples with the main difference being the evolution of the bands with time-on-stream. The high ratio of cyclic to linear species - represented in the right axis of Fig. S6 as the intensity ratio of the 515 nm/555 nm bands [55] - is in line with the strong, initial Brønsted acidity of both the

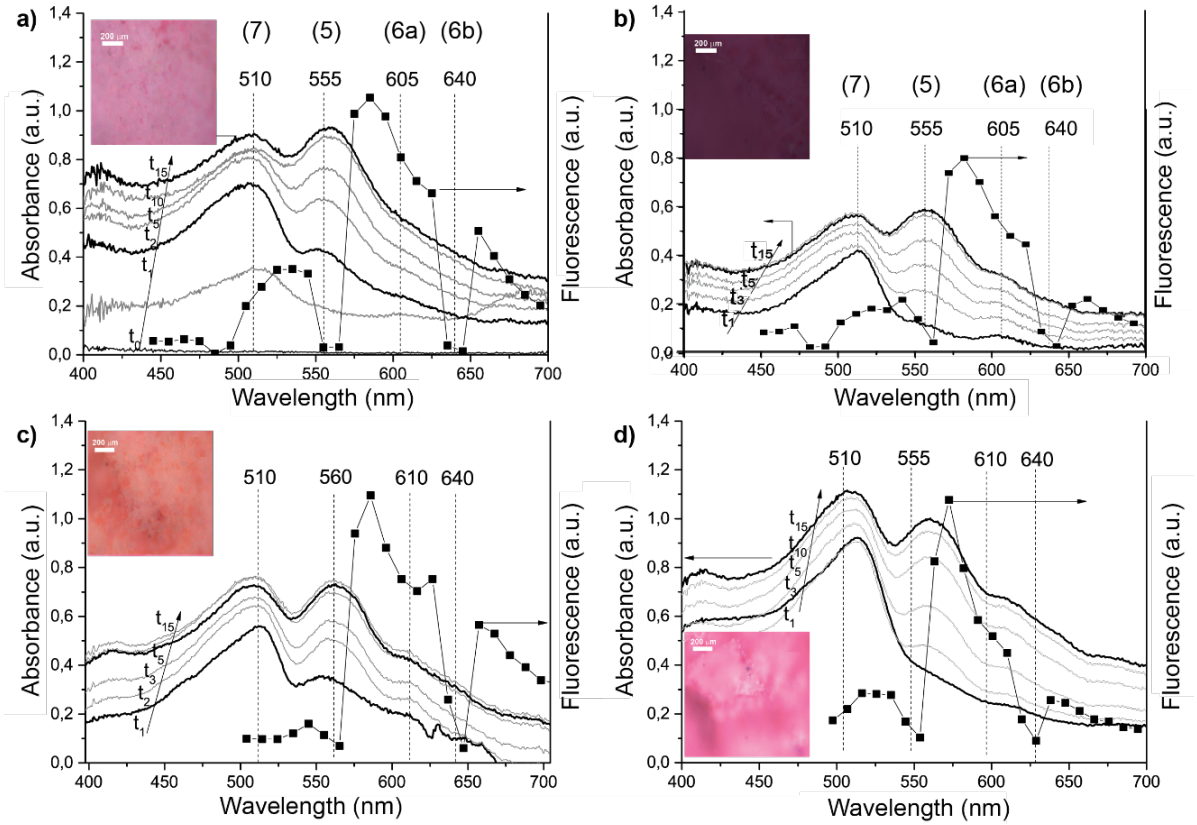

Fig. 4 Evolution of UV-Vis absorption spectra (continuous line) and ex-situ (30 min after reaction) fluorescence spectra (scattered line) of the 4-fluorostyrene oligomerization reaction products recorded at 100 °C for: (a) h-ZSM-5; b) ZrO_2/h-ZSM-5; c) n-ZSM-5; d) ZrO_2/n-ZSM-5. Excitation lasers are fixed at λ = 488, 561, 642 nm. Insets are optical images of the corresponding samples after 15 min of 4-fluorostyrene oligomerization.

Green Chemistry

ARTICLE

h-ZSM-5 and n-ZSM-5 zeolites, as shown by Py-FTIR. The staining results confirm that the Brønsted acidity initially present in the pure zeolites is partially preserved after ZrO_2 impregnation. The fact that less of higher oligomers, denoted as 6a and 6b species, are seen for the ZrO_2 impregnated zeolites (Fig. 4 and Fig. S6a-b, c-d) would be in line with less accessible acid sites compared to the parent sample, in particular for the hierarchical zeolite.

While the final UV-Vis spectra of h-ZSM-5 and n-ZSM-5 are very similar (despite their different Si/Al ratios), the time profiles of 5 and 7 (Fig. S6) are rather different. Indeed, the reaction seemed to occur faster on the nano-sized zeolite, likely because of better diffusivity, with the concentration profiles plateauing much faster. This result confirms the existence of a partial micropore blockage in the h-ZSM5 sample, provoked by the high concentration of extra-framework Al species, which is further enhanced by Zr incorporation, as concluded above from the Ar adsorption-desorption isotherms. Likewise, the optical images of the samples after staining and reaction are included in insets in Fig. 4, showing pink colouration of all samples, except for the ZrO_2/h-ZSM-5 material, which looks purple. The pink colour, over purple, indicates the presence of more cyclic species (7), visually confirming the observation made by Py-FTIR that ZrO_2/h-ZSM-5 has less strong BAS accessible to the pyridine molecules.

Biomass catalytic pyrolysis tests

Wheat-straw was employed as biomass feedstock representative of agriculture residues. Prior to the pyrolysis tests, it was subjected to acid washing (WS-ac) to minimize any possible interference associated with indigenously catalytic components naturally present in the raw biomass, such as alkali and alkali earth metals (AAEM) [56]. The catalytic pyrolysis experiments were performed in a two-zone reactor in which the thermal and catalytic conversions take place at different temperatures (550 and 400 °C, respectively), allowing optimization of the bio-oil production in each step. The different catalysts were tested using two catalyst/biomass ratios (0.4 and 0.7 g/g) in order to obtain results at two levels of bio-oil upgrading. With this configuration, the residual solid fraction (char) formed in the thermal conversion zone was very similar in all cases, with a mass yield of around 19 wt%. This product originated entirely from the initial biomass devolatilization and was retained in the upper reactor zone, avoiding direct contact with the catalyst bed.

Products distribution and bio-oil oxygen content. Fig. 5a depicts the product distribution in terms of mass yield for the catalytic pyrolysis of WS-ac employing the two ZSM-5 supports (n-ZSM-5 and h-ZSM-5) with a catalyst to biomass ratio of 0.7. The products include the organic part of the bio-oil (denoted as bio-oil*), the non-condensable gases, water and the coke deposited over the catalyst. Fig. 5b shows the oxygen content of the bio-oil* obtained in the different pyrolysis experiments, whereas Fig. 5c illustrates the mass yield corresponding to the different components present in the gas fraction: CO, CO_2, CH_4, gaseous olefins (GO) and gaseous paraffins (GP). As reference, the results corresponding to a pure thermal test are also included in this figure.

As expected, the incorporation of the zeolite catalyst bed for upgrading the bio-oil vapours causes strong changes in both the product distribution and the bio-oil* oxygen content compared to the pure thermal test, showing a high catalytic activity of the two ZSM-5 catalysts here employed. Thus, a notable reduction in the bio-oil* oxygen content is observed from the thermal bio-oil* to the catalytic ones. Note that the thermal bio-oil* presents an oxygen content (39 wt%) quite close to that of the raw biomass (42.8 wt%), indicating that a pure thermal degradation is poorly effective for deoxygenating the liquid organic fraction. In contrast, the use of ZSM-5 catalysts led to the production of bio-oils* with less oxygen, in the range of 20.7 – 27.3 wt% according to the data shown in Fig. 5b. However, the bio-oil* upgrading by catalytic deoxygenation was accompanied by a strong decrease in the bio-oil* yield at the expense of the enhanced formation of gases and water, as well as of the appearance of a new solid fraction (coke) deposited over catalysts. Within the non-condensable gases, the zeolite catalysts increased strongly the formation of CO, CO_2 and gaseous olefins (mainly propylene), with a more moderate effect on the yields of methane and other gaseous paraffins. The enhanced formation of water, CO and CO_2 occurred in agreement with the bio-oil* deoxygenation by dehydration, decarbonylation and decarboxylation routes, respectively. Likewise, the strong increase in the production of light hydrocarbons, in particular of gaseous olefins, over the zeolite catalysts reflects that these materials also promote severe cracking reactions, which are detrimental for the bio-oil* yield. Methane has earlier been proposed to originate mainly from the lignin biopolymer [12] by demethylation of the abundant methoxyl groups in the lignin structure. On the other hand, gaseous olefins may be formed through decarbonylation of light oxygenated intermediates or by cracking of alkyl aromatics [57].

Interesting differences can be denoted in Fig. 5 between the product distribution obtained over both zeolitic supports (n-ZSM-5 and h-ZSM-5), mainly regarding the bio-oil* yield and its oxygen content. Thus, the n-ZSM-5 sample produces more bio-oil* than the h-ZSM-5 material, and with a significantly lower

Green Chemistry

ARTICLE

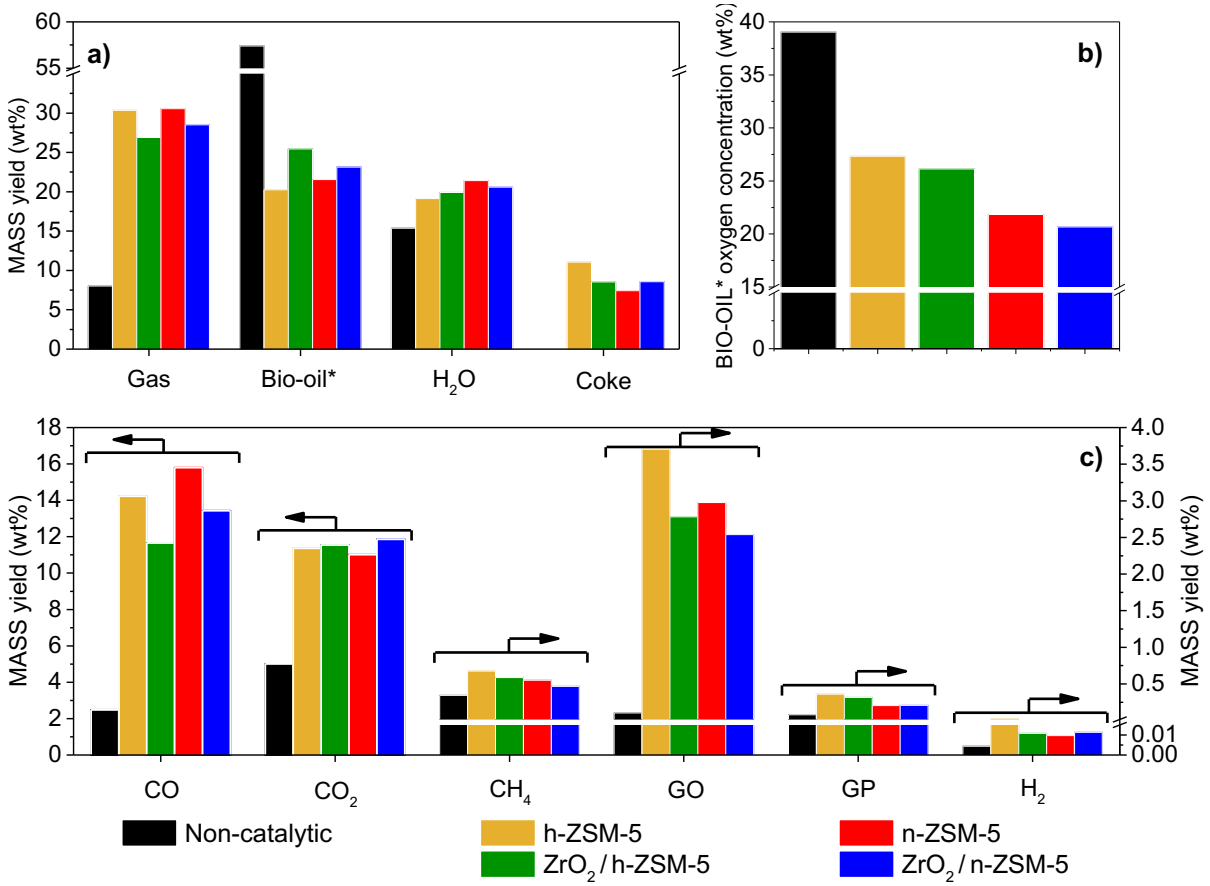

Fig. 5 Products yield distribution (wt%) (a), Bio-oil oxygen concentration (wt%, dry basis) (b) and gaseous components yield (wt%) (c), in the fast-pyrolysis of WS-ac (Catalyst/Biomass = 0.7 g/g, T = 550/400 °C). GO: gaseous olefins (C_2–C_4); GP: gaseous paraffins (C_2–C_4).

oxygen content, showing its superior properties for bio-oil* upgrading.

The variation in the bio-oil* production can be manly related to the higher acid site concentration in h-ZSM-5 sample, which promotes the generation of more gases and the formation of more of coke deposits. Increased coking causes a faster zeolite deactivation, explaining the lower bio-oil* deoxygenation degree achieved with the hierarchical ZSM-5 sample.

The results obtained in biomass catalytic pyrolysis when incorporating ZrO_2 over the two ZSM-5 samples have been also included in Fig. 5. For both supports the addition of Zr positively affected bio-oil* yield while reducing the gas production, with minor variations in water formation. Interestingly, this enhanced production of bio-oil* is accompanied by a small but noticeable reduction in its oxygen content. Within the gas fraction, Zr-incorporation decreased mainly the production of CO and CH_4, with little changes in the case of CO_2, gaseous olefins and paraffins. Moreover, for the h-ZSM-5 sample, Zr modification also reduced coke deposition over the catalyst attenuating its deactivation. These results can be directly related to the fine tuning of the zeolite acidity by Zr incorporation, since it reduces the concentration of strong acid sites, limiting undesired severe cracking and coking reactions.

Deoxygenation selectivity. The oxygen contained in the raw biomass and, subsequently, in the bio-oil* can be removed by a variety of reactions that can be grouped into three main routes, depending on the final product that contains the oxygen atoms: dehydration, decarbonylation and decarboxylation. Least preferred is decarbonylation as it brings a significant loss of both mass and energy yield of the bio-oil*. In term of mass, the oxygen removal through decarbonylation involves the formation of one molecule of CO containing 57.1 wt% of oxygen, i.e. it takes place with a 42.9 wt% carbon loss. In contrast, for decarboxylation and dehydration the respective oxygen contents in CO_2 and H_2O are 72.7 and 88.9 wt% O, which implies considerably lower mass losses of C and H, respectively. Regarding the chemical energy yield, decarbonylation is also a less favourable route compared to

decarboxylation and dehydration, since CO still contains a significant heating value (12.6 MJ·Nm^{-3}). Thus, the term overall deoxygenation selectivity is defined as the mass of oxygen removed from the original biomass by means of CO, CO_2 and H_2O. By subtracting the thermal overall deoxygenation contribution to those of the catalytic experiments, catalytic deoxygenation selectivity was calculated in a similar way.

Taking into account the yield of H_2O, CO and CO_2 obtained in the different biomass pyrolysis tests, as well as their oxygen content, the overall deoxygenation selectivity is shown in Fig. 6a. For non-catalytic biomass pyrolysis, the major pathway was dehydration (with a selectivity of 72%), followed by decarboxylation and with a minor contribution of decarbonylation. Nevertheless, it must be taken into account that in the thermal experiment deoxygenation has little effect on the bio-oil* fraction since its oxygen content is just slightly lower than that of the raw biomass. This means that in the non-catalytic pyrolysis the observed deoxygenation pathways are really surpassed for the formation of char, which shows reduced oxygen content compared to the raw biomass, as concluded previously [9].

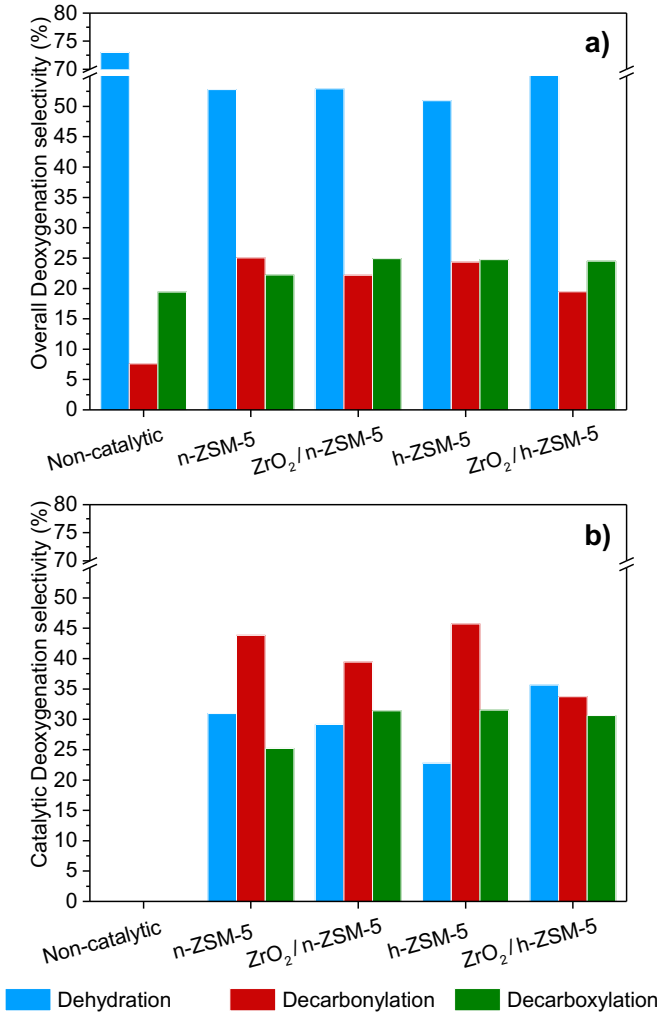

Fig. 6 Overall deoxygenation (a) and catalytic deoxygenation (b) selectivity in the fast-pyrolysis of WS-ac. (Catalyst/Biomass = 0.7 g/g, T = 550/400 °C).

For the catalytic experiments, dehydration is still the main overall deoxygenation route, although a larger contribution of decarboxylation and in particular of decarbonylation is observed. By subtracting the thermal contribution to the overall production of H_2O, CO and CO_2, it was possible to assess the catalytic deoxygenation selectivity, as shown in Fig. 6b. For both ZSM-5 supports, decarbonylation is the predominant route of catalytic deoxygenation, followed by dehydration (over n-ZSM-5) or decarboxylation (over h-ZSM-5). Decarbonylation selectivity was higher for the hierarchical ZSM-5 sample, reaching a value of 45.7%. These facts highlight one of the limitations of ZSM-5 zeolite for efficiently upgrading bio-oil as it promotes the least favourable deoxygenation route, i.e. decarboxylation. However, the addition of Zr to the zeolitic supports, and associated moderation of strong BAS in ZSM-5 zeolites, reduced decarbonylation selectivity, which is a positive effect in terms of both mass an energy yields of the remaining bio-oil* fraction. This result was more pronounced in the case of the h-ZSM-5 sample.

Energy yield distribution. Since typically the main goal of biomass catalytic pyrolysis is the production of biofuels, one important parameter is how the chemical energy initially present in the biomass is distributed among the different fractions obtained. In this way, Fig. 7 shows the chemical energy distribution per fraction corresponding to the experiments performed with a catalyst/biomass ratio of 0.7, including also the results corresponding to the thermal test.

In the thermal, non-catalytic experiment, almost 70% of the biomass chemical energy is present in the bio-oil* fraction and just a small proportion in the gases. The remainder of the chemical energy is contained in the char produced in the pyrolysis process due to its relatively low oxygen content.

For the catalytic pyrolysis tests, sharp changes are observed in the energy yield distribution. Thus, the h-ZSM-5 and n-ZSM-5 parent zeolites exhibit a relatively low bio-oil* energy yield, with values almost half of that corresponding to the thermal bio-oil, as a great part of the chemical energy is contained in

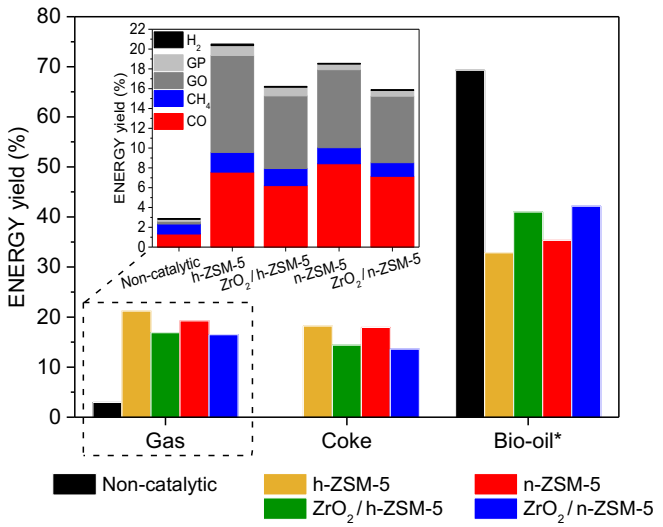

Fig. 7 Energy yield distribution (%) in the fast-pyrolysis of WS-ac. (Catalyst/Biomass = 0.7 g/g, T = 550/400 °C). GO: gaseous olefins (C_2–C_4); GP: gaseous paraffins (C_2–C_4).

the coke, CO and gaseous olefins formed. This finding denotes the relevance of, not only having a favourable deoxygenation pathway, but also of avoiding the formation of coke and gaseous hydrocarbons during biomass catalytic pyrolysis in order to minimize the bio-oil* energy yield losses during the upgrading process.

Zr incorporation onto both ZSM-5 zeolitic supports had a positive effect on the bio-oil* energy yield, with their modified acidity being responsible for the improved biomass catalytic pyrolysis with lower production of coke, light hydrocarbons and CO.

Bio-oil upgrading efficiency. The above results show that bio-oil* deoxygenation over zeolite catalysts is accompanied by a sharp decrease in both mass and energy yield of this fraction. To make a proper comparison between the different catalysts, both parameters must be assessed together. Fig. 8 illustrates the evolution of the bio-oil* oxygen content versus the mass and energy yields, respectively, of the bio-oil* fraction. For each catalyst, the results obtained operating at two different catalyst/biomass ratios (0.4 and 0.7 g/g, respectively) have been represented in this figure to illustrate the corresponding bio-oil* upgrading pathways. As expected, regardless of the

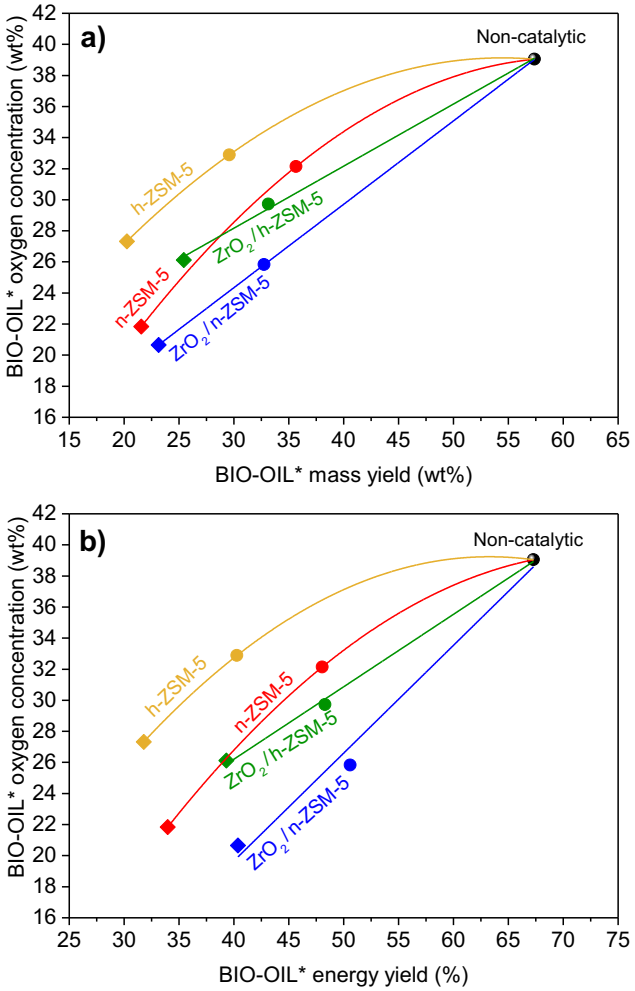

Fig. 8 Bio-oil* oxygen concentration versus bio-oil* mass (a) and energy (b) yields obtained in the fast-pyrolysis of WS-ac varying the catalyst to biomass ratio (T = 550/400 °C).

zeolite used, a higher catalyst to biomass ratio led to a reduction of the bio-oil* oxygen concentration, although also causing a decrease in the bio-oil* yield. The trend of the curves varies significantly depending on the catalyst employed, which in turn is a result of the efficiency of each material for promoting deoxygenation without paying too much of a penalty in terms of mass and energy yields of the bio-oil* fraction.

The data in Fig. 8 confirm that the n-ZSM-5 support is superior in all cases than the h-ZSM-5 one for catalytic biomass pyrolysis, affording the production of bio-oils* with higher deoxygenation degrees and with higher/superior yields. The microcrystalline h-ZSM-5 zeolite, prepared by desilication hence showing a low Si/Al ratio, was not very efficient at bio-oil upgrading: it led to a strong reduction in the bio-oil* yield with just moderate deoxygenation, due to the occurrence of undesired reactions, as seen in previous sections. On the other hand, this figure illustrates clearly how for the two ZSM-5 supports the incorporation of Zr had a very positive effect, as it improves both the bio-oil* yield and its deoxygenation degree. The ZrO_2/n-ZSM-5 sample was the most efficient, allowing the production of a highly deoxygenated bio-oil* while reducing the mass and energy losses due to secondary transformations. Thus, for a catalyst/biomass ratio of 0.7 g/g, this catalytic system was able to decrease the bio-oil* oxygen concentration to reach a value as low as 20 wt% containing still 40% of the biomass chemical energy. Compared to the thermal bio-oil*, these figures show that the oxygen content is halved, retaining about 60% of its chemical energy.

Bio-oil GC-MS composition. Due to numerous compounds present in the bio-oil, GC-MS is often applied as a semi-quantitative tool for product distribution analysis, based on relative area%, in spite of the large variation between their response factors. Moreover, it is known that the compounds identified by GC-MS represent just a fraction of the total components contained in the bio-oil* sample. In particular, oligomers derived from the partial fragmentation of the three biopolymers in lignocellulose cannot be detected by GC-MS. To avoid these problems, in this work the most abundant components in the different organic products families have been quantified after calibration, allowing the results to be provided as mass yield relative to the initial raw biomass weight. Likewise, from the elemental composition of the quantified matter, its contribution in terms of chemical energy yield was determined. The results obtained from the GC-MS analyses of the bio-oil* produced over the catalysts based on the nanocrystalline ZSM-5 material are shown in Fig. 9 and compared with the thermal bio-oil*.

Bio-oil obtained in the absence of any catalysts consists mainly of not quantified matter, which accounts for about 70% of the total in this sample (Fig. 9a). This result denotes the high content of oligomers in the non-catalytic bio-oil*, showing the limitations of a pure thermal treatment in achieving a total fragmentation of the lignocellulose biopolymers.

In the case of the catalytic pyrolysis tests, Fig. 9a shows that while the overall bio-oil* yield dropped upon addition of the n-ZSM-5 catalyst to the reaction system, the amount of non-

quantified matter was significantly reduced, this effect being nhanced at higher catalyst/biomass ratios. This fact highlights the ability of ZSM-5 zeolite to convert the biomass oligomers, although this transformation is not really very efficient from the point of view of upgraded bio-oil* production, as the yield corresponding to the quantified matter does not improve compared to the thermal experiment. Accordingly, it can be concluded that the n-ZSM-5 sample promotes the conversion of the oligomers mainly through non-desired secondary reactions, leading to the formation of gaseous hydrocarbons, CO and carbonaceous residues.

However, this picture is quite different when analysing the results obtained over the ZrO_2/n-ZSM-5 sample. With this catalyst, the reduction in the oligomers is accompanied by an enhancement of the mass yield into the quantified components. This variation is more pronounced when the comparison is made in terms of chemical energy yield due to the high deoxygenation degree of the bio-oil* produced. Therefore, the presence of Zr species over the catalyst and, in particular of new Lewis acid sites, provides it with a remarkable catalytic activity for converting the biomass oligomers into smaller components in the bio-oil* fraction, overcoming the limitations of the parent ZSM-5 support. Thus, for a catalyst/biomass ratio of 0.7 g/g, the ZrO_2/n-ZSM-5 catalyst leads to the production of a bio-oil* with little oligomers, achieving simultaneously a reduction to half of the oxygen content shown by the thermal bio-oil.

The yields of the main components present in the quantified fraction of the bio-oil are shown in Fig. 9b. Products have been classified according to the following families: carboxylic acids (AC), light oxygenates (LO: aldehydes, ketones, ethers and alcohols), furans (FUR), oxygenated aromatics (O-AR), aromatic hydrocarbons (AR) and anhydrosugars (SUG). For the thermal bio-oil, the major components by far are the anhydrosugars (mainly levoglucosan), with also significant yields of other compounds families such LO and O-AR. In contrast, any hydrocarbons present in this bio-oil fall below the detection limit. In a previous work [9], a simplified reaction mechanism scheme was proposed to account for the main transformation routes occurring during the biomass catalytic fast-pyrolysis. According to this scheme, levoglucosan, furans and oxygenated aromatics are considered to be the main products coming from the depolymerisation of cellulose, hemicellulose and lignin, respectively. Their subsequent conversion leads to the formation of other families of oxygenated species, such as carboxylic acids, ketones and ethers.

As expected, bio-oil product distribution was strongly affected by the incorporation of the n-ZSM-5 catalyst to the reaction system, this effect being more pronounced for the experiment performed at the highest catalyst/biomass ratio. Thus, for the catalytic bio-oil* SUG is no longer the major fraction as levoglucosan is almost completely converted, probably by dehydration into furans [58,59]. In the same way, the yield corresponding to most of the other oxygenated compounds families (AC, LO and FUR) decreased in the case of the catalytic pyrolysis tests upon increasing the catalyst/biomass ratio. However, this is not the case for O-AR since its yield increases when working at the highest catalyst/biomass ratio. On the other hand, while the thermal bio-oil* does not contain any appreciable amount of hydrocarbons, the n-ZSM-5 catalyst led to the appearance of aromatic hydrocarbons. According to the literature [9,60,61], one of the predominant pathways for the formation of these aromatic hydrocarbons consists of first the dehydration of levoglucosan into furans, followed by Diels-Alder condensation of the latter with light alkenes, mainly propylene, which are present in significant amounts in the non-condensable gas fraction. Nevertheless, the contribution of a carbon-pool type mechanism cannot be discarded in the formation of aromatic hydrocarbons.

Interestingly, the modification of the n-ZSM-5 zeolite with ZrO_2 had a profound effect on the product distribution shown in Fig. 9b. For both catalyst/biomass ratios, an increase in the yield of all families of oxygenated compounds is observed compared to the pure ZSM-5 support, in agreement with the ability of the ZrO_2-modified catalysts to promote the conversion of the oligomers present in the bio-oil. These enhanced yields are

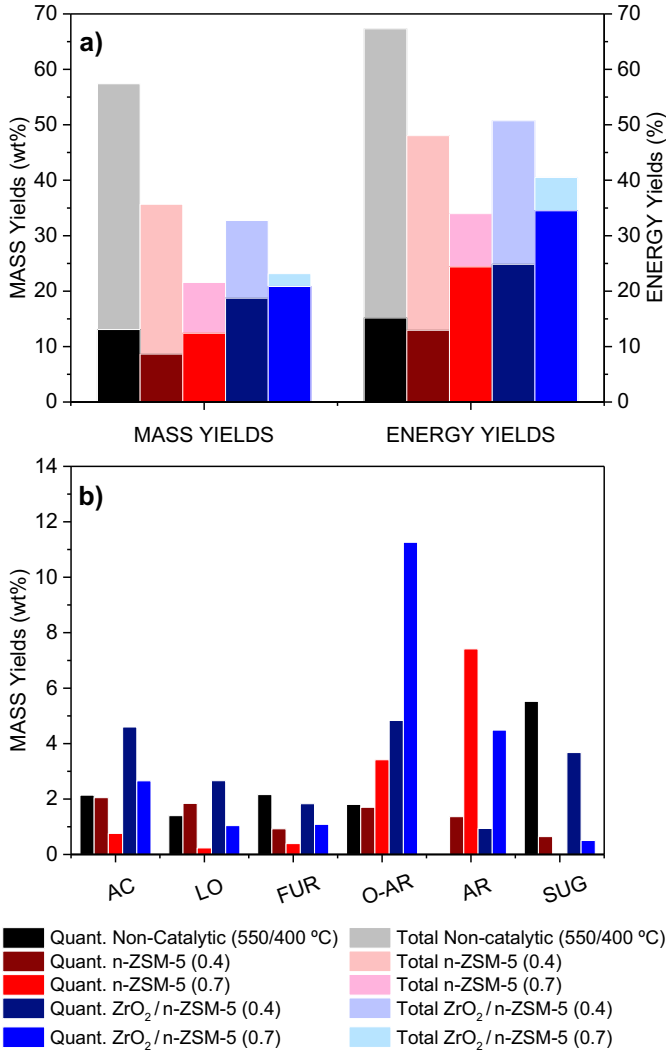

Fig. 9 Total/Quantified bio-oil* components (a), and bio-oil* components mass yields in terms of main organic compounds families (b) obtained in the fast-pyrolysis of WS-ac (Catalyst to biomass weight ratio indicated in brackets, T = 550/400 °C).

particularly remarkable in the case of oxygenated aromatics and, to a lesser extent, for carboxylic acids (consisting mainly of acetic acid), which can be interpreted as a direct result of the conversion of oligomers into smaller compounds, catalysed by the new types of Lewis acid sites generated upon ZrO_2 incorporation. Accordingly, a remarkable overall upgrading of the bio-oil* fraction is achieved when using the Zr-modified n-ZSM-5 sample.

Conclusions

Nanosized and hierarchical ZSM-5 zeolites, showing enhanced accessibility, have been investigated in biomass catalytic pyrolysis to promote the conversion and upgrading of the bulky molecules coming from the thermal fragmentation of the lignocellulose biopolymers into partially deoxygenated bio-oil*. Acid washed wheat straw (WS-ac) has been used as a feedstock representative of agriculture wastes. The tests have been performed in an ex-situ catalytic pyrolysis system, which allows the thermal and catalytic steps to operate under different, previously optimised reaction temperatures.

In spite of the favourable accessibility of these ZSM-5 samples, they still suffer from a number of limitations in biomass catalytic pyrolysis that negatively affect the bio-oil* yield. The excessive presence of strong acid sites in ZSM-5 zeolite favours the occurrence of undesired reactions, such as severe cracking leading to gaseous hydrocarbons and the formation of carbonaceous residues over the catalyst, causing its deactivation. Moreover, among the different deoxygenation pathways, the ZSM-5 zeolite extensively promotes decarbonylation, which is undesired as it results in a significant loss of both mass and energy yields of the bio-oil*. Regarding the composition of the liquid organic fraction, the ZSM-5 catalysts are able to transform a great part of the oligomers present in the bio-oil* compared to the non-catalytic test, significantly increasing the components detected by GC-MS. However, even by working at high catalyst/biomass ratio, the parent ZSM-5 samples cannot completely convert those oligomers, which negatively affects the bio-oil* properties.

Incorporation of Zr to the ZSM-5 supports, in the form of highly dispersed species, modifies the ZSM-5 physicochemical properties and strongly improves its catalytic performance for biomass catalytic pyrolysis. The addition of Zr allows the zeolite acidity to be adjusted, decreasing the concentration of the strong acid sites linked to the zeolitic support and generating a new type of Lewis acid sites associated with the highly dispersed ZrO_2 phase. This effect is more pronounced for the nanocrystalline ZSM-5 catalyst since in this material Zr is mainly in the form of very small ZrO_2 nanoparticles distributed over the external surface of the zeolite crystals. The modification of ZSM-5 with Zr leads to enhanced bio-oil* yields combined with a high deoxygenation degree, as a result of: a decrease in severe cracking reactions, less coke formation and reduction in the extent of deoxygenation by decarbonylation. Moreover, the Zr-modified catalysts show considerably better activity for the conversion of the oligomers present in the bio-oil*, suggesting the participation of the new population of Lewis acid sites in these reactions. The best results are obtained with the ZrO_2/n-ZSM-5 catalyst, which show the highest bio-oil* yields in terms of both mass and chemical energy, producing a partially deoxygenated liquid organic fraction with low content of oligomeric species.

Conflicts of interest

There are no conflicts to declare.

Acknowledgements

The authors gratefully acknowledge the financial support from: the European Union Seventh Framework Programme (FP7/2007–2013) under grant agreement nº 604307 (CASCATBEL project), and from the Spanish Ministry of Economy and Competitiveness through CATPLASBIO project (Ref: CTQ2014-602209-R). J. Čejka thanks the Czech Science Foundation for the financial support (P106/12/G015). Likewise, the authors thank SILKEM company for the preparation and supply of the hierarchical ZSM-5 sample. The NMR studies were supported by NWO (Middelgrootprogram, grant number 700.58.102 to MB).

Notes and references

1 J. Fermoso, P. Pizarro, J. M. Coronado and D. P. Serrano, *Adv. Rev.*, 2017, **6**, 1–18.
2 J. Fermoso, P. Pizarro, J. M. Coronado and D. P. Serrano, in *Encyclopedia of Sustainability Science and Technology*, ed. R. A. Meyers, Springer, New York, 2017, pp. 1–33.
3 D. Carpenter, T. L. Westover, S. Czernik and W. Jablonski, *Green Chem.*, 2014, **16**, 384–406.
4 A. V Bridgwater, *Biomass and Bioenergy*, 2011, **38**, 68–94.
5 D. Mohan, C. U. Pittman and P. H. Steele, *Energy & Fuels*, 2006, **20**, 848–889.
6 R. H. Venderbosch, *ChemSusChem*, 2015, **8**, 1306–1316.
7 A. V. Bridgwater, *Catal. Today*, 1996, **29**, 285–295.
8 Z. Cao, J. Engelhardt, M. Dierks, M. T. Clough, G. H. Wang, E. Heracleous, A. Lappas, R. Rinaldi and F. Schï¿½th, *Angew. Chemie - Int. Ed.*, 2017, **56**, 2334–2339.
9 H. Hernando, S. Jiménez-Sánchez, J. Fermoso, P. Pizarro, J. M. Coronado and D. P. Serrano, *Catal. Sci. Technol.*, 2016, **6**, 2829–2843.
10 Y. Zheng, F. Wang, X. Yang, Y. Huang, C. Liu, Z. Zheng and J. Gu, *J. Anal. Appl. Pyrolysis*, 2017, **126**, 169–179.
11 liangyuan Jia, M. Raad, S. Hamieh, J. Toufaily, T. Hamieh, M. Bettahar, G. Mauviel, M. Tarrighi, L. Pinard and A. Dufour, *Green Chem.*, 2017, **19**, 5442–5459.
12 K. Wang, K. H. Kim and R. C. Brown, *Green Chem.*, 2014, **16**, 727–735.
13 Á. Ibarra, A. Veloso, J. Bilbao, J. M. Arandes and P. Castaño, *Appl. Catal. B Environ.*, 2016, **182**, 336–346.
14 G. Pacchioni, *ACS Catal.*, 2014, **4**, 2874–2888.
15 K. Wu, M. Yang, W. Pu, Y. Wu, Y. Shi and H. sheng Hu, *ACS Sustain. Chem. Eng.*, 2017, **5**, 3509–3516.

16 J. Wang, B. Zhang, Z. Zhong, K. Ding, A. Deng, M. Min, P. Chen and R. Ruan, *Energy Convers. Manag.*, 2017, **139**, 222–231.

17 S. Tosoni, H. T. Chen, R. Puigdollers and G. Pacchioni, *Philos. Trans. R. Soc. A - Math. Phys. Eng. Sci.*, 2018, **376**, 1–19.

18 C. Liu, H. Wang, A. M. Karim, J. Sun and Y. Wang, *Chem. Soc. Rev.*, 2014, **43**, 7594–7623.

19 S. Wan and Y. Wang, *Front. Chem. Sci. Eng.*, 2014, **8**, 280–294.

20 A. Galadima and O. Muraza, *Energy Convers. Manag.*, 2015, **105**, 338–354.

21 D. Fabbri, C. Torri and V. Baravelli, *J. Anal. Appl. Pyrolysis*, 2007, **80**, 24–29.

22 Y. T. Cheng, J. Jae, J. Shi, W. Fan and G. W. Huber, *Angew. Chem. Int. Ed.*, 2012, **51**, 1387–1390.

23 T. C. Hoff, M. J. Holmes, J. Proano-Aviles, L. Emdadi, D. Liu, R. C. Brown and J. P. Tessonnier, *ACS Sustain. Chem. Eng.*, 2017, **5**, 8766–8776.

24 C. Hu, R. Xiao and H. Zhang, *Bioresour. Technol.*, 2017, **243**, 1133–1140.

25 A. A. Lappas, K. G. Kalogiannis, E. F. Iliopoulou, K. S. Triantafyllidis and S. D. Stefanidis, *Wiley Interdiscip. Rev. Energy Environ.*, 2012, **1**, 285–297.

26 D. Kubička, I. Kubičková and J. Čejka, *Catal. Rev. Sci. Eng.*, 2013, **55**, 1–78.

27 A. Zheng, Z. Zhao, S. Chang, Z. Huang, H. Wu, X. Wang, F. He and H. Li, *J. Mol. Catal. A Chem.*, 2014, **383**–**384**, 23–30.

28 J. Li, X. Li, G. Zhou, W. Wang, C. Wang, S. Komarneni and Y. Wang, *Appl. Catal. A Gen.*, 2014, **470**, 115–122.

29 K. Qiao, X. Shi, F. Zhou, H. Chen, J. Fu, H. Ma and H. Huang, *Appl. Catal. A Gen.*, 2017, **547**, 274–282.

30 J. Fermoso, H. Hernando, P. Jana, I. Moreno, J. Přech, C. Ochoa-Hernández, P. Pizarro, J. M. Coronado, J. Čejka and D. P. Serrano, *Catal. Today*, 2016, **277**, 171–181.

31 B. Valle, A. G. Gayubo, A. T. Aguayo, M. Olazar and J. Bilbao, *Energy & Fuels*, 2010, **24**, 2060–2070.

32 P. Li, X. Chen, X. Wang, J. Shao, G. Lin, H. Yang, Q. Yang and H. Chen, *Energy and Fuels*, 2017, **31**, 3979–3986.

33 M. M. Yung, A. R. Stanton, K. Iisa, R. J. French, K. A. Orton and K. A. Magrini, *Energy & Fuels*, 2016, **30**, 9471–9479.

34 L. Sun, X. Zhang, L. Chen, B. Zhao, S. Yang and X. Xie, *J. Anal. Appl. Pyrolysis*, 2016, **121**, 342–346.

35 M. M. Yung, A. K. Starace, C. Mukarakate, A. M. Crow, M. A. Leshnov and K. A. Magrini, *Energy and Fuels*, 2016, **30**, 5259–5268.

36 P. He, W. Shan, Y. Xiao and H. Song, *Top. Catal.*, 2016, **59**, 86–93.

37 H. Zhang, J. Zheng and R. Xiao, *BioResources*, 2013, **8**, 5612–5621.

38 W. W. Purwato, D. Supramono, R. Muthia and M. F. Firdaus, *Int. J. Technol.*, 2015, **7**, 1069–1075.

39 P. Li, D. Li, H. Yang, X. Wang and H. Chen, *Energy & Fuels*, 2016, **30**, 3004–3013.

40 W. Shen, G. A. Tompsett, K. D. Hammond, R. Xing, F. Dogan, C. P. Grey, W. C. Conner, S. M. Auerbach and G. W. Huber, *Appl. Catal. A Gen.*, 2011, **392**, 57–68.

41 D. Liang, G. Li, Y. Liu, J. Wu and X. Zhang, *Catal. Commun.*, 2016, **81**, 33–36.

42 S. Wang and E. Iglesia, *J. Phys. Chem. C*, 2016, **120**, 21589–21616.

43 M. Signoretto, F. Menegazzo, L. Contessotto, F. Pinna, M. Manzoli and F. Boccuzzi, *Appl. Catal. B Environ.*, 2013, **129**, 287–293.

44 N. Korsunska, V. Papusha, O. Kolomys, V. Strelchuk, A. Kuchuk, V. Kladko, Y. Bacherikov, T. Konstantinova and L. Khomenkova, *Phys. Status Solidi Curr. Top. Solid State Phys.*, 2014, **11**, 1417–1422.

45 R. Fricke, H. Kosslick, V. A. Tuan, I. Grohman, W. Pilz, W. Storek and G. Walther, in *Studies in Surface Science and Catalysis*, 1994, vol. 83, pp. 57–66.

46 E. Djurado, F. Boulc, L. Dessemond, N. Rosman and M. Mermoux, *J. Electrochem. Soc.*, 2004, **151**, 774–780.

47 H. Wang, G. Li, Y. Xue and L. Li, *J. Solid State Chem.*, 2007, **180**, 2790–2797.

48 M. Hunger, in *Zeolite Characterization and Catalysis. A Tutorial*, eds. A. W. Chester and E. G. Derouane, Springer, 2009, pp. 65–105.

49 L. Rodríguez-González, F. Hermes, M. Bertmer, E. Rodríguez-Castellón, A. Jiménez-López and U. Simon, *Appl. Catal. A Gen.*, 2007, **328**, 174–182.

50 A. Samoson, E. Lippmaa, G. Engelhardt, U. Lohse and H.-G. Jerschkewitz, *Chem. Phys. Lett.*, 1987, **134**, 589–592.

51 Z. Yan, D. Ma, J. Zhuang, X. Liu, X. Liu, X. Han, X. Bao, F. Chang, L. Xu and Z. Liu, *J. Mol. Catal. A Chem.*, 2003, **194**, 153–167.

52 C. Poupin, R. Maache, L. Pirault-Roy, R. Brahmi and C. T. Williams, *Appl. Catal. A Gen.*, 2014, **475**, 363–370.

53 I. L. C. Buurmans, E. a Pidko, J. M. de Groot, E. Stavitski, R. a van Santen and B. M. Weckhuysen, *Phys. Chem. Chem. Phys.*, 2010, **12**, 7032–7040.

54 Z. Ristanović, A. V. Kubarev, J. Hofkens, M. B. J. Roeffaers and B. M. Weckhuysen, *J. Am. Chem. Soc.*, 2016, **138**, 13586–13596.

55 L. R. Aramburo, S. Wirick, P. S. Miedema, I. L. C. Buurmans, F. M. F. de Groot and B. M. Weckhuysen, *Phys. Chem. Chem. Phys.*, 2012, **14**, 6967–6973.

56 J. Fermoso, H. Hernando, S. Jiménez-sánchez, A. A. Lappas, E. Heracleous, P. Pizarro, J. M. Coronado and D. P. Serrano, *Fuel Process. Technol.*, 2017, **167**, 563–574.

57 A. Corma, G. Huber, L. Sauvanaud and P. Oconnor, *J. Catal.*, 2007, **247**, 307–327.

58 T. Carlson, J. Jae, Y. Lin, G. Tompsett and G. Huber, *J. Catal.*, 2010, **270**, 110–124.

59 X. Zhang, K. Wilson and A. F. Lee, *Chem. Rev.*, 2016, **116**, 12328–12368.

60 Y.-T. Cheng and G. W. Huber, *Green Chem.*, 2012, **14**, 3114–3125.

61 A. Fukutome, H. Kawamoto and S. Saka, *ChemSusChem*, 2015, **8**, 2240–2249.